




Hydrogen passivated V_{Zn} - Ga_{Zn} complexes as major defects in Ga-doped ZnO nanowires evidenced by x-ray linear dichroism and density functional theory

Eirini Sarigiannidou,^{1,*} Pierre Gaffuri,¹ Fabrice Wilhelm ,² Joseph Kioseoglou ,³ Andrei Rogalev,² Efstratios Nikidis,³ Estelle Appert,¹ and Vincent Consonni ¹

¹Université Grenoble Alpes, CNRS, Grenoble INP, LMGP, 38016 Grenoble, France

²European Synchrotron Radiation Facility (ESRF), 71 avenue des Martyrs, 38043 Grenoble, France

³Physics Department, Aristotle University of Thessaloniki, 54124 Thessaloniki, Greece



(Received 17 January 2023; accepted 5 June 2023; published 17 July 2023)

The elucidation of the residual and intentional doping processes in ZnO nanowires (NWs) grown by chemical bath deposition (CBD) is a major but still largely unexplored issue despite its primary importance for many nanoscale engineering devices. Here, we investigate the local structural environment around Ga dopants in ZnO NWs by combining synchrotron radiation-based x-ray linear dichroism with density functional theory calculations. We show that the family of V_{Zn} - Ga_{Zn} - nH defect complexes is predominantly formed and hence that hydrogen acts as an efficient passivating species even for intentional dopants like Ga. The residual and intentional doping processes are found to be highly correlated through significant interplay effects. These findings revisit the nature of intentional dopant-induced defects and defect complexes in ZnO NWs. They further reveal that hydrogen should be considered in unintentionally doped ZnO NWs grown by CBD as major defects but also in intentionally doped ZnO NWs through its efficient passivating effect, opening perspectives to more finely control their optical and electrical properties.

DOI: [10.1103/PhysRevMaterials.7.076001](https://doi.org/10.1103/PhysRevMaterials.7.076001)

I. INTRODUCTION

The development of ZnO nanowires (NWs) by chemical bath deposition (CBD) [1,2] has received great attention over the past decades for a wide variety of engineering devices [3–9]. However, while the structural morphology of ZnO NWs including their shape, verticality, and dimensions (e.g., length, diameter) has been optimized on many types of substrates [10,11], the control over their optical and electrical properties has not yet been achieved. This significantly reduces the performance of devices made of ZnO NWs. In that respect, the residual and intentional doping processes of ZnO NWs grown by CBD along with their possible interaction are still valuable but largely unknown.

Generally, the issue of native defects and hydrogen in ZnO has been highly debated, and consensus has emerged from experimental and theoretical data [12,13]. The Zn vacancy (V_{Zn}) has been found to be the dominant negatively charged native defect using positron annihilation experiments [14]. From density functional theory (DFT) calculations, V_{Zn} is known to exhibit a low formation energy when the Fermi level is close to the conduction band minimum (CBM) and to be the most favorable native point defect specifically under intermediate and oxygen-rich conditions [15]. It acts as a deep acceptor with a -2 charge state [15] and presents a typical emission line ~ 1.6 eV using optical spectroscopy [16]. In addition to the role of V_{Zn} , hydrogen-related defects including

interstitial hydrogen in bond-centered sites (H_{BC}) [17] and substitutional hydrogen on the oxygen sites (H_O) [18] have been shown to be the source of the n -type conductivity of ZnO [19], excluding the role of the oxygen vacancy (V_O) acting as a deep donor [20]. H_{BC} and H_O with $+1$ charge states act as two shallow donors with a very low formation energy, regardless of the Fermi level in the band gap [17,18]. Moreover, several types of defect complexes related to V_{Zn} and interstitial hydrogen (H_i) [20–22] as well as to substitutional nitrogen on the oxygen sites (N_O) [23–27] have been investigated experimentally and by DFT calculations, and in all cases, the charge state is considered from $+2$ down to -2 due to the implication of V_{Zn} . More recently, it has also been suggested that hydrogen may combine with intentional dopants such as group III-A elements to form more complicated defect complexes [21].

Based on that well-established knowledge, the residual and intentional doping processes of ZnO NWs grown by CBD as the currently most important deposition technique are largely unknown and strongly affected by the aqueous medium, which is polar and contains a large amount of hydrogen and nitrogen. On the one hand, a couple of recent reports have shown that hydrogen is massively incorporated into ZnO NWs when grown by CBD through a residual doping process [28,29] and forms many defects including H_{BC} and V_{Zn} -3H complexes [22,27]. On the other hand, following the optimization of the process conditions during CBD, several dopants including Al [30], Ga [31], Cu [32], and Sb [33] have been incorporated into ZnO NWs through an intentional doping process. Among them, Ga acting as a shallow donor [34] is one of the most investigated dopants in ZnO NWs

*eirini.sarigiannidou@grenoble-inp.fr

owing to its high potential in the fields of optoelectronics [31,35–39]. Following both statements, one of the most important and yet open questions relies on how the residual and intentional doping processes interact each other and hence affect the local atomic structure around the intentional dopants incorporated into ZnO NWs. This open question is crucial, as the local atomic structure governs the electrical activity of intentional dopants and hence the doping efficiency in ZnO NWs, but it has never been explored owing to the inherent experimental limitations.

The accurate and precise determination of the local atomic structure around an intentional dopant is a prerequisite to control the physical properties of ZnO NWs and hence to tune the macroscopic response to different solicitations for engineering devices. X-ray diffraction, x-ray photoelectron spectroscopy, high-resolution transmission electron microscopy, Raman spectroscopy, and x-ray absorption spectroscopy (XAS) can provide detailed information on the local electronic and atomic structure. Nevertheless, discriminating the nature of dopant-induced defects that are present in a host lattice still constitutes a challenging task. XAS provides a set of element-specific probes that are suitable for studying thin films and nanomaterials. For example, x-ray absorption near edge structure (XANES) and extended x-ray absorption fine structures (EXAFS) have extensively been used to reveal the presence of cobalt vacancy-related complexes in Co-doped ZnO films [40] or V_{Zn} in Cu-doped ZnO-diluted magnetic semiconductor films [41]. However, the sensitivity of those methods relies on the small modifications of the relative intensity of all the spectral features of the XANES measurements or on the complicated data treatment within EXAFS analysis. In contrast, x-ray linear dichroism (XLD) allows us to probe the local structural environment, and as a differential spectroscopy method, it is inherently a very sensitive characterization technique. The power of XLD was demonstrated on Mn-doped GaN films [42] and then on Co-doped ZnO films [43] to quantitatively assess the fraction of the absorbing atomic species incorporated at a specific lattice site in diluted magnetic semiconductors. Until now, a comprehensive investigation of the local atomic structure of Ga-doped ZnO NWs is practically nonexistent in the literature despite its primary importance.

In this paper, to establish the correlation between the residual and intentional doping processes, a full description of the local structural environment around Ga dopants in ZnO NWs grown by CBD is studied by XLD measurements recorded at the Zn and Ga K-edges using synchrotron-based x-ray radiation. Structural models of intentional dopant-induced defects and defect complexes in ZnO are investigated by DFT calculations. The resulting relaxed atomic structures are then used as input data for XANES and XLD simulations and confronted with the recorded experimental XANES and XLD spectra, respectively. We demonstrate that hydrogen passivated V_{Zn} -Ga $_{Zn}$ defect complexes are the predominantly major defects in ZnO NWs grown by CBD. These findings revisit the nature of intentional dopant-induced defects and defect complexes in ZnO NWs grown by CBD, emphasizing the need to consider hydrogen as an efficient passivating species.

II. EXPERIMENTAL AND THEORETICAL DETAILS

A. Synthesis method

Ga-doped ZnO NW arrays were grown on (001) silicon (Si) wafers using a two-step chemical synthesis process as described in Ref. [31]. First, a *c*-axis-oriented polycrystalline ZnO seed layer was deposited by dip coating. The prepared solution, an equimolar mix of 375 mM of both zinc acetate dihydrate $[Zn(CH_3COO)_2 \cdot 2H_2O]$, Emsure ACS] and monoethanolamine (MEA, Sigma-Aldrich) in pure ethanol, was heated and stirred at 60 °C for 12 h and then remained for 12 h more at the room temperature. The xerogel film was formed by dipping the Si wafer in the solution and withdrawn at the speed of 3.3 mm/s in ambient atmosphere with controlled hygrometry measured <15%. The xerogel film was annealed in air on a hot plate first at 300 °C for 1 h to evaporate the solvent and organic residues and then at 500 °C for 3 h to achieve its crystallization. Secondly, vertically *c*-axis-oriented Ga-doped ZnO NWs were grown by CBD. The ZnO seed-layer-coated silicon wafer was immersed face down in a sealed beaker containing an equimolar mix of 30 mM zinc nitrate hexahydrate $[Zn(NO_3)_2 \cdot 6H_2O]$, Sigma-Aldrich] and HMTA ($C_6H_{12}N_4$, Sigma-Aldrich) in deionized water, together with 0.75 mM of gallium nitrate hydrate $[Ga(NO_3)_3 \cdot xH_2O]$, Sigma-Aldrich]. The pH of the solution prior to heating was equal to 10.9 by the addition of 584 mM of ammonia (NH_3 , VWR Chemicals). The sealed beaker containing the solution was placed in a regular oven heated at 85 °C for 3 h. Both the pH and temperature of the solution were monitored in an *in situ* manner to follow their variation as CBD proceeded.

B. Characterization techniques

The pH and temperature of the solution as CBD proceeded were monitored in an *in situ* manner using an InLab Versatile Pro pH electrode from Mettler Toledo. The morphology and structural properties of ZnO NWs were measured by top- and cross-sectional-view field emission scanning electron microscopy (FESEM) images using a FEI Quanta 250 field emission gun scanning electron microscope. The Ga incorporation into ZnO NW arrays was investigated by energy-dispersive x-ray spectroscopy (EDS) analyses and Raman scattering measurements. FESEM-EDS spectra of ZnO NW arrays were collected using a Bruker x-ray detector incorporated into the FEI Quanta 250 FESEM instrument operating at 20 kV. Scanning transmission electron microscopy (STEM) specimens were prepared by scratching the surface of ZnO NW arrays using a diamond tip and spread on a Cu grid. STEM-EDS spectra and maps of single ZnO NWs were recorded with a JEOL SDD Centurio detector incorporated into a JEOL 2100F FESEM instrument operating at 200 kV and having a 0.2 nm resolution in the scanning mode. Raman scattering measurements were performed using a Horiba/Jobin Yvon Labram spectrometer equipped with a liquid-nitrogen-cooled charge-coupled device detector. The 488 nm excitation line of an Ar^+ laser was used with the power on the sample surface <10 mW. The laser beam was focused to a spot size of $1 \mu m^2$ using a 50× long working

distance objective. The spectra were calibrated in wave numbers at room temperature by using a silicon reference sample and considering that the theoretical position of the silicon Raman line was set to 520.7 cm^{-1} .

C. XANES and XLD measurements

XANES measurements were carried out at the ID12 beamline at the European Synchrotron Radiation Facility (ESRF) in Grenoble (France) [44]. The XANES was recorded for two orthogonal linear polarizations. A 0.9-mm-thick diamond quarter wave plate was used to flip the linearly polarized x-rays several times at each energy point from vertical to horizontal by converting the incoming circularly polarized x-rays emitted by the second harmonic of the HELIOS-II type HU52 and APPLE-II type HU38 helical undulators at the Zn and Ga K-edges, respectively. To reduce the heat load of the first harmonic of the helical undulators, $100\text{ }\mu\text{m}$ Al foil was inserted ahead of the Si(111) double-crystal monochromator. The sample was measured at 10° grazing incidence, i.e., vertical linear polarization strictly perpendicular to the c -axis direction (the E vector of the light \perp to the c axis) of the NWs, whereas the horizontal linear polarization is close to the c -axis direction (E vector $\parallel c$). For the Zn and Ga K-edges, total fluorescence yield (TFY) was used as the detection system. Additionally, the XANES spectrum at the Zn K-edge was also measured with the total electron yield and used as a reference for correcting the self-absorption effects of the XANES spectra measured in TFY. The XLD was then taken as the direct difference of the normalized XANES with $E\perp c$ and $E\parallel c$. The isotropic XANES was derived from the weighted average of the two spectra, i.e., $[2 \times \text{XANES}(E\perp c) + \text{XANES}(E\parallel c)]/3$. The XANES and XLD spectra at the Zn and Ga K-edges were simulated using the *ab initio* FDMNES code [45,46]. For both the Zn and Ga K-edges, the calculations were performed using the finite difference method (FDM). Self-consistency and relativistic effects were not included in the calculations since the agreement between the experimental and theoretical XANES and XLD spectra was not improved. As the $3d$ electron shells for both Zn and Ga are full ($3d^{10}$), quadrupolar transitions were not included. For the FDMNES simulations, we used the relaxed structural models calculated previously from VASP. The convergence of the FDMNES calculations was checked for increasing cluster sizes, and only minor evolutions were found for cluster radii $>9.0\text{ }\text{\AA}$. The simulated in-plane XANES component is taken as the average over the different in-plane axes since the NWs are randomly oriented in-plane. The simulated spectra were convoluted using a steplike energy-dependent broadening. The steplike energy-dependent broadening was centered at $\sim 20\text{ eV}$ above the inflection point of the XANES for both Zn and Ga K-edges. The core-hole lifetime of 1.67 eV for Zn, 1.82 eV for Ga, the experimental energy resolution (1.3 eV), and a thermic disorder using the Debye model to damp the EXAFS part of the XAS spectrum were considered for the convolution. The simulated XLD spectra were rescaled by a factor of ~ 0.6 , and the corresponding XANES spectra for both linear polarizations were then recalculated. Using this procedure, better agreement regarding the spectral shape with the experimental data was reached for both XLD and XANES spectra at the Zn K-edge.

D. DFT calculations

The investigation of the wurtzite ZnO structure was performed using the VASP code [47,48] with projector augmented-wave potentials [49] under the Perdew-Burke-Ernzerhof derivation of the generalized gradient approximation (GGA-PBE) [50,51] of DFT. The reciprocal-space resolution for k-point mesh generation was set by a Monkhorst-Pack mesh of $8 \times 8 \times 6$ for the $1 \times 1 \times 1$ unit cell, while the k-point mesh is Γ centered, and the cutoff energy is set at 600 eV . For this paper, a $4 \times 4 \times 3$ cell consisting of 192 atoms was considered, while convergence with respect to k-point sampling and slab and vacuum thickness was explicitly checked. Extensive tests concluded that smaller cells are insufficient for the structural relaxation and accurate calculations of the optoelectronic properties of the point defects in ZnO. Reliable optical properties require an accurate determination of the electronic band gap. Hence, the DFT + U method was used to accurately calculate the electronic and optical properties. The DFT + U approach is better at describing systems with localized d and f electrons. A strong intra-atomic interaction was introduced in a screened manner as an on-site replacement of DFT. In this paper, the simplified rotationally invariant approach to DFT + U introduced in Ref. [52] was used. Initially, U was incorporated only for the d states of Zn, and the $U_{d,\text{Zn}}$ was set to 7.5 , a parameter that produces good lattice constants and significantly improves the band gap of ZnO from 0.70 to 1.85 eV , as reported in Ref. [53]. Nevertheless, it was shown in Ref. [54] that the correct band gap can be obtained if, in addition to the U values for the d states, U values are considered also for the s or p state. The corresponding U values were obtained from Refs. [55,56]: $U_{d,\text{Zn}} = 10.5\text{ eV}$ and $U_{p,\text{O}} = 7.0\text{ eV}$. It should be noted that the lattice constants are slightly underestimated. In addition, to accurately reproduce the electronic properties of $\beta\text{-Ga}_2\text{O}_3$, $U_{d,\text{Ga}} = 7.0\text{ eV}$ was used consistent with our previous studies and the literature [57].

Mainly in the previous related studies, significantly smaller supercells of 72 atoms [34] and 96 atoms [21] were used with hybrid functionals. It is well known that the formation energies are significantly higher using the + U method than using the hybrid functionals calculations. This difference is mainly due to the valence band maximum (VBM) position shift on the absolute energy scale. In the + U extrapolation approach, it is assumed that the VBM was well described. However, hybrid functional calculations showed that the VBM shifted down by $\sim 1.7\text{ eV}$ compared with GGA calculations [58], likely due to self-interaction corrections to the valence band states not considered in the + U method [59]. As a result, the VBM has an additional downward shift of $\sim 1.5\text{ eV}$ compared with the + U method [59].

In general, in this paper, the calculated heat of formation is much larger than previous calculations due to the GGA + U approach that we have implemented. Previous GGA DFT-based calculations concluded that the $\varepsilon(1+)$ transition level of Ga_{Zn} is at 1.5 eV above the VBM, while by the use of different + U with respect to ours, the transition level is found at 2.1 eV or by using the extrapolation formula at 3.9 eV [60] from the VBM. The band gap extrapolation formula of Janotti and Van de Walle [15] was used to extrapolate the

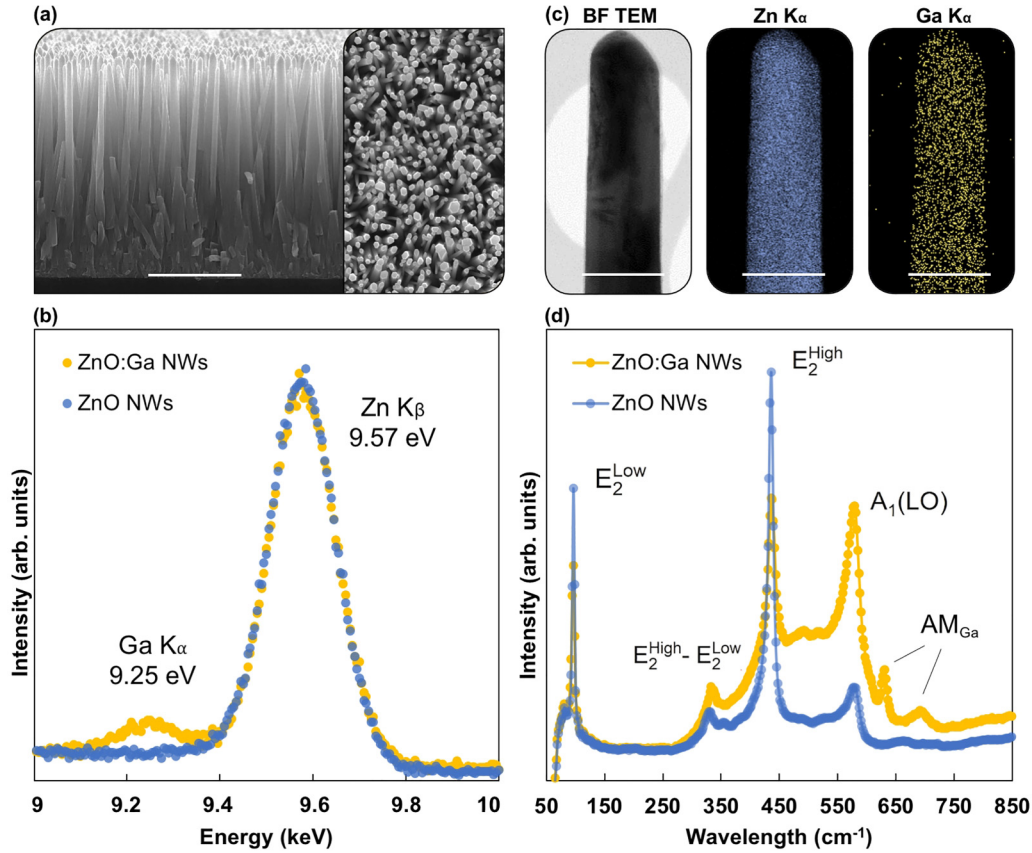


FIG. 1. (a) Cross-sectional and top-view field emission scanning electron microscopy (FESEM) images of Ga-doped ZnO nanowires (NWs). The scale bar is 2 μm . (b) FESEM-EDS spectra of nonintentionally doped and Ga-doped ZnO NWs. Both spectra were normalized with respect to the Zn K β line pointed at 9.57 keV. (c) Bright-field transmission electron microscopy (TEM) image and scanning transmission electron microscopy (STEM)-energy-dispersive x-ray spectroscopy (EDS) elemental maps of Zn and Ga atoms, respectively, collected on a single Ga-doped ZnO NW. The scale bar is 200 nm. (d) Raman scattering spectra of nonintentionally doped and Ga-doped ZnO NWs.

band gap following the DFT + U approach to the experimentally calculated value of 3.4 eV in ZnO. Following the band gap extrapolation formula, the transition energy levels depend linearly on + U as follows:

$$\varepsilon\left(\frac{q}{q'}\right) = \varepsilon\left(\frac{q}{q'}\right)^{\text{DFT}+U} + \frac{\Delta\varepsilon}{\Delta E_g}(E_g^{\text{exp}} - E_g^{\text{DFT}+U}), \quad (1)$$

where

$$\frac{\Delta\varepsilon}{\Delta E_g} = \frac{\varepsilon\left(\frac{q}{q'}\right)^{\text{DFT}+U} - \varepsilon\left(\frac{q}{q'}\right)^{\text{DFT}}}{E_g^{\text{DFT}+U} - E_g^{\text{DFT}}}. \quad (2)$$

However, in this paper, the DFT + U approach calculates the correct experimental band gap energy value (3.4 eV). Hence, our calculated transition energy levels correspond to those found in the literature when using the band gap extrapolation formula of Janotti and Van de Walle [15]. However, by the use of hybrid functionals [34], the $\varepsilon(1 + /0)$ transition level is found at 3 eV from the VBM, while in this paper, it is found above the CBM, indicating that Ga $_{\text{Zn}}$ acts as a shallow donor, in agreement with Ref. [60].

III. RESULTS AND DISCUSSION

The addition of Ga(NO $_3$) $_3$ in the chemical bath is a typical way to intentionally dope ZnO NWs with Ga using CBD. In the high pH region, Ga(OH) $_4^-$ complexes are predominantly formed in the chemical bath and adsorb on the positively charged nonpolar m -plane sidewalls of ZnO NWs following attractive electrostatic forces. The adsorption process is favorable for the incorporation process of Ga dopants into ZnO NWs but also alters the development of the m -plane sidewalls by notably increasing the radial growth. The structural morphology and physicochemical properties of Ga-doped ZnO NWs are presented in Fig. 1. Ga-doped ZnO NWs are vertically aligned on top of the c -axis-oriented ZnO seed layer and exhibit a relatively flat faceted hexagonal tip, as seen in Fig. 1(a). They have a mean length and diameter of $\sim 4 \mu\text{m}$ and 100 nm with an apparent density of $\sim 40 \text{ NW}/\mu\text{m}^2$. By using a [Ga(NO $_3$) $_3$]/[Zn(NO $_3$) $_2$] ratio of 2.5%, ZnO NWs are significantly doped with Ga, as shown by the Ga K α line located at 9.25 eV in Fig. 1(c). A high Ga/Zn element ratio of $\sim 1.5\text{--}2\%$ is measured using the FESEM-EDS analysis. The spatial distribution of Ga dopants in ZnO NWs is further homogeneous, as seen in Fig. 1(b). The incorporation process of Ga is also indicated by the increase in the intensity of the A $_1(\text{LO})$ line at 574 cm $^{-1}$ and by the presence of additional

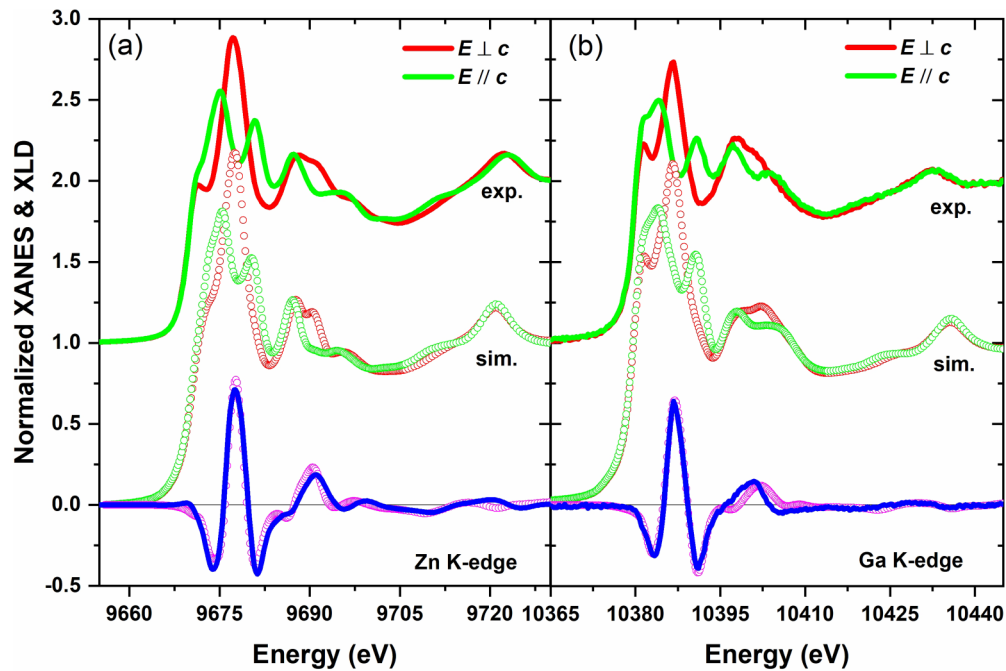


FIG. 2. Experimental (solid lines) and simulated (open symbols) normalized x-ray absorption near edge structure (XANES) spectra recorded with two orthogonal linear polarizations and the corresponding x-ray linear dichroism (XLD) spectra for Ga-doped ZnO nanowires (NWs) at the (a) Zn K-edge and (b) Ga K-edge.

modes (AM_{Ga}) located at 633.5 and 696.1 cm^{-1} , as presented in Fig. 1(d). These particularities are strongly characteristic of the effective doping of ZnO NWs with Ga. Additionally, the crystallinity of Ga-doped ZnO NWs is high, as indicated by the intense, narrow E_2^{High} line at $\sim 438\text{ cm}^{-1}$, and no extended defects are formed following the incorporation process of Ga, as shown in the transmission electron microscopy (TEM) image analysis.

Figure 2(a) presents the experimental XANES and XLD spectra recorded at the Zn K-edge of Ga-doped ZnO NWs. A clear anisotropy of the XANES spectra is observed and gives rise to a strong XLD signal. The spectral shape of the XLD spectrum is typical for the ZnO wurtzite structure, i.e., a tetrahedral coordination of the Zn^{2+} cation to the surrounding O^{2-} anions. The spectral shape as well as the amplitude of the XLD signal ($\sim 71\%$ at the maximum) is identical to ZnO-based samples [43]. This strongly indicates that the incorporation of Ga dopants with a concentration of $\sim 1.5\text{--}2\%$ into ZnO NWs hardly disturbs the overall bulk wurtzite structure. The open circle lines in Fig. 2(a) show the FDMNES simulated Zn K-edge XANES and XLD spectra. They were calculated using a pure ZnO wurtzite structure with the bulk lattice parameters of $a = 3.2496\text{ \AA}$ and $c = 5.2042\text{ \AA}$ from Ref. [61] and a dimensionless u parameter of 0.382 from Ref. [62]. The simulated spectra reproduce very well the experimental one, especially the energy positions and relative amplitudes of the individual peaks in the XANES and thus the XLD spectra. Compared with FDMNES simulations done within the muffin-tin approximation, the rising edge is better reproduced with the FDM except the first small positive peak in the XLD at 9.67 keV [63]. The excellent agreement between the experimental data and simulations done with

FDMNES at the Zn K-edge for a pure ZnO wurtzite structure validates the method to be followed when switching to the Ga K-edge. This is in good agreement with the estimation made by comparing the edge jump of Zn and Ga K-edges, see the Supplemental Material [64].

Figure 2(b) displays the XANES and the respective XLD spectra recorded at the Ga K-edge of Ga-doped ZnO NWs. The spectral shape of both XANES and XLD spectra is nearly like the Zn K-edge one, suggesting that Ga dopants substitute for the Zn sites. This can be proven with the help of simulations where Ga dopants can be intentionally placed in different sites within the crystal lattice, i.e., as a substitutional dopant in a Zn site (Ga_{Zn}), as a substitutional dopant in an O site (Ga_O), on an interstitial site (Ga_i), or when creating defect complexes involving hydrogen atoms. To simulate the XANES and XLD spectra, the relaxed atomic structures determined by DFT calculations were used as input data.

From Fig. 3, where the resulting simulated XANES and XLD spectra at the Ga K-edge with a Ga^{2+} electronic state are grouped, it is obvious that the large majority of Ga dopants substitute for the Zn sites since the contribution of the positive peak located at 10380 eV for Ga_i and Ga_O is not observed in the experimental XLD spectrum. Those experimental results are also confirmed from total energy calculations, where Ga_i and Ga_O are energetically unfavorable by $>6\text{ eV}$ under moderate conditions for the neutral charge state.

Knowing that the concentration of V_{Zn} is considerable in ZnO NWs grown by CBD and that they can form defect complexes affecting their electrical conductivity [22], we wanted to investigate and provide clear experimental evidence about the role of the defect complex V_{Zn} - Ga_{Zn} , i.e., the proximity of Ga_{Zn} with respect to V_{Zn} . Many reports have shown that

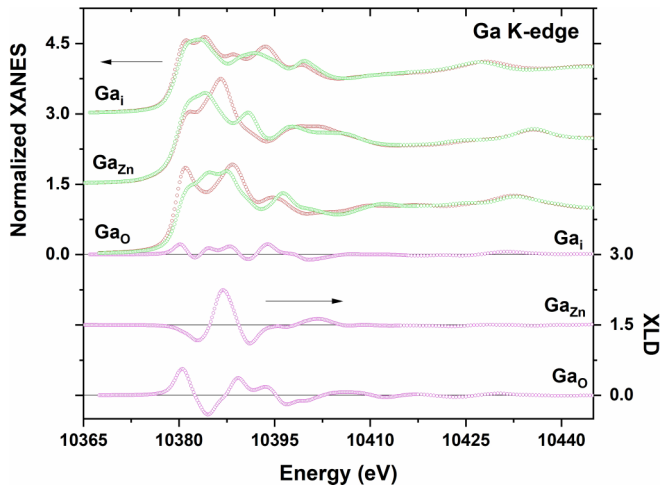


FIG. 3. Simulated x-ray absorption near edge structure (XANES) spectra (left scale) for the two orthogonal linear polarizations at the Ga K-edge and the corresponding x-ray linear dichroism (XLD) spectrum (right scale) for three different positions of Ga in the ZnO lattice structure: Ga in a Zn site (Ga_{Zn}), Ga in an O (Ga_{O}) site, and Ga in an interstitial position (Ga_{i}). All XANES spectra are normalized to unity and shifted to each other for the sake of clarity.

the XANES signal is sensitive to structural defects [40], but most of them are solely based on the use of only one linear polarization, i.e., only changes in the XANES spectrum but not in the XLD spectrum that is *a fortiori* more sensitive. Moreover, to consider the crystallographic characteristics of the wurtzite structure, basal as well as axial, along the c axis, possible atomic positions of the Ga dopants are studied theoretically by DFT calculations. Two positions of Ga_{Zn} on the basal plane $\text{V}_{\text{Zn}}\text{-Ga}_{\text{Zn}}\text{-B}$ are examined. The first one $\text{V}_{\text{Zn}}\text{-Ga}_{\text{Zn}}\text{-B1}$, where Ga_{Zn} is bonded in the first coordination shell (i.e., first neighbor distance) to an undercoordinated O atom due to V_{Zn} , and the second one $\text{V}_{\text{Zn}}\text{-Ga}_{\text{Zn}}\text{-B2}$, where Ga_{Zn} is bonded in the second coordination shell (i.e., in second neighbor distance) to the undercoordinated O atoms. Similarly, concerning the axial direction, the two following cases are considered: the first one $\text{V}_{\text{Zn}}\text{-Ga}_{\text{Zn}}\text{-A1}$, where Ga_{Zn} is bonded in the first coordination shell to an undercoordinated O atom above V_{Zn} , and the second one $\text{V}_{\text{Zn}}\text{-Ga}_{\text{Zn}}\text{-A2}$, where Ga_{Zn} is bonded in the second coordination shell to the undercoordinated O atoms, i.e., in a c -lattice parameter distance with respect to the V_{Zn} . For each of the four cases, five distinct charge cases were considered within the DFT calculations using the VASP code. The neutral as well as the $+2$, $+1$, -1 , and -2 charge cases are designed by removing 2 or 1 and adding 1 or 2 electrons, respectively. Those cases are denoted as, e.g., $\text{V}_{\text{Zn}}\text{-Ga}_{\text{Zn}}\text{-A1}^{+2}$, $\text{V}_{\text{Zn}}\text{-Ga}_{\text{Zn}}\text{-A1}^{+1}$, $\text{V}_{\text{Zn}}\text{-Ga}_{\text{Zn}}\text{-A1}^0$, $\text{V}_{\text{Zn}}\text{-Ga}_{\text{Zn}}\text{-A1}^{-1}$, and $\text{V}_{\text{Zn}}\text{-Ga}_{\text{Zn}}\text{-A1}^{-2}$. From DFT calculations, Ga_{Zn} close to V_{Zn} either in axial A1 or basal B1 positions are found to be energetically favorable [Figs. 4(a) and 4(b), respectively]. Concerning the axial A and basal B possible Ga sites, the axial one [Fig. 4(a)] is energetically favorable for neutral and negative charge states, while the basal one [Fig. 4(b)] is energetically favorable for positive charge states. Regarding Ga_{Zn} in axial A position,

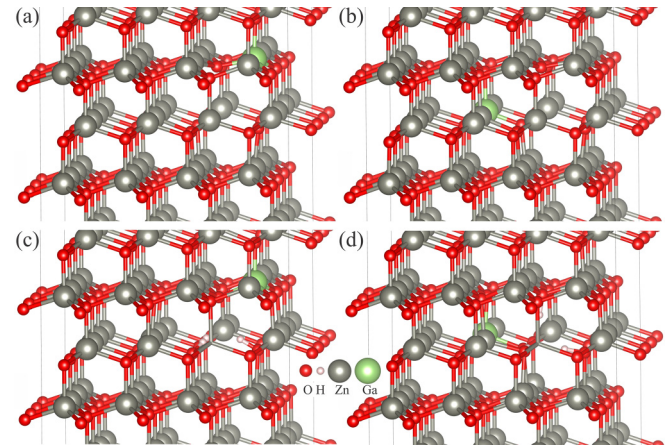


FIG. 4. Relaxed structural models for the most stable atomic configurations of $\text{V}_{\text{Zn}}\text{-Ga}_{\text{Zn}}$ and $\text{V}_{\text{Zn}}\text{-Ga}_{\text{Zn}}\text{-}n\text{H}$ defect complexes. In (a), the axial $\text{V}_{\text{Zn}}\text{-Ga}_{\text{Zn}}\text{-A1}$ defect complex is represented. In (b), the basal $\text{V}_{\text{Zn}}\text{-Ga}_{\text{Zn}}\text{-B1}$ defect complex is represented. In (c), the $\text{V}_{\text{Zn}}\text{-Ga}_{\text{Zn}}\text{-A1}_3\text{HB}$ defect complex is represented, where the Ga_{Zn} lies in the axial A1 position and all three hydrogen atoms lie in the basal B positions. In (d), the $\text{V}_{\text{Zn}}\text{-Ga}_{\text{Zn}}\text{-B1}_3\text{H2B1A}$ defect complex is represented, where the Ga_{Zn} lies in the basal B1 position, two hydrogen atoms lie in the basal B positions, and one hydrogen atom lies in the axial A position. Large gray balls, small red balls, and large green balls denote Zn, O, and Ga atoms, respectively. Small white balls are hydrogen atoms. The Zn atom in front of V_{Zn} was taken out for the sake of clarity, and only its bonds with the neighboring O atoms are represented.

having all hydrogen atoms in basal B positions is the most energetically favorable configuration (3HB, 2HB, and HB) [Fig. 4(c)], while regarding Ga_{Zn} in basal B position, sharing hydrogen atoms in basal B and axial A positions is energetically favorable (3H2B1A and 2HBA) [Fig. 4(d)].

Figure 5(a) shows the simulated XANES spectra for the four different positions of V_{Zn} using the relaxed structural models denoted as $\text{V}_{\text{Zn}}\text{-Ga}_{\text{Zn}}\text{-B1}$, $\text{V}_{\text{Zn}}\text{-Ga}_{\text{Zn}}\text{-B2}$, $\text{V}_{\text{Zn}}\text{-Ga}_{\text{Zn}}\text{-A1}$, and $\text{V}_{\text{Zn}}\text{-Ga}_{\text{Zn}}\text{-A2}$. For the sake of simplicity, the simulated XLD spectra were convoluted with only the Ga core-hole lifetime. Although the presence of V_{Zn} does not affect the overall shape of the XLD spectra, important differences occur at the beginning of the spectra, i.e., just above the Fermi level with the first negative peak marked by an asterisk in Fig. 5(a). This makes the comparison between the different spectra possible. The fact that the overall shape of the XLD spectra remains similar is related to the fact that the introduction of V_{Zn} keeps the wurtzite structure unchanged, and the lattice parameter after relaxation of the cell is within 0.01 \AA , like the pristine one. It should be emphasized that most of the differences arise from V_{Zn} and are not due to the change of the averaged nearest-neighbor interatomic distance. The small structural modification as well as the change in the u parameter (within $\pm 1\%$) have an insignificant influence on the shape of the XLD spectra. Furthermore, the electronic state of the Ga dopants remains Ga^{2+} . The largest change on the XLD spectrum is seen when V_{Zn} is in axial A position, either A1 or A2. The first negative peak located at 10380 eV in the simulated XLD spectrum for $\text{V}_{\text{Zn}}\text{-Ga}_{\text{Zn}}\text{-A1}$ is hardly

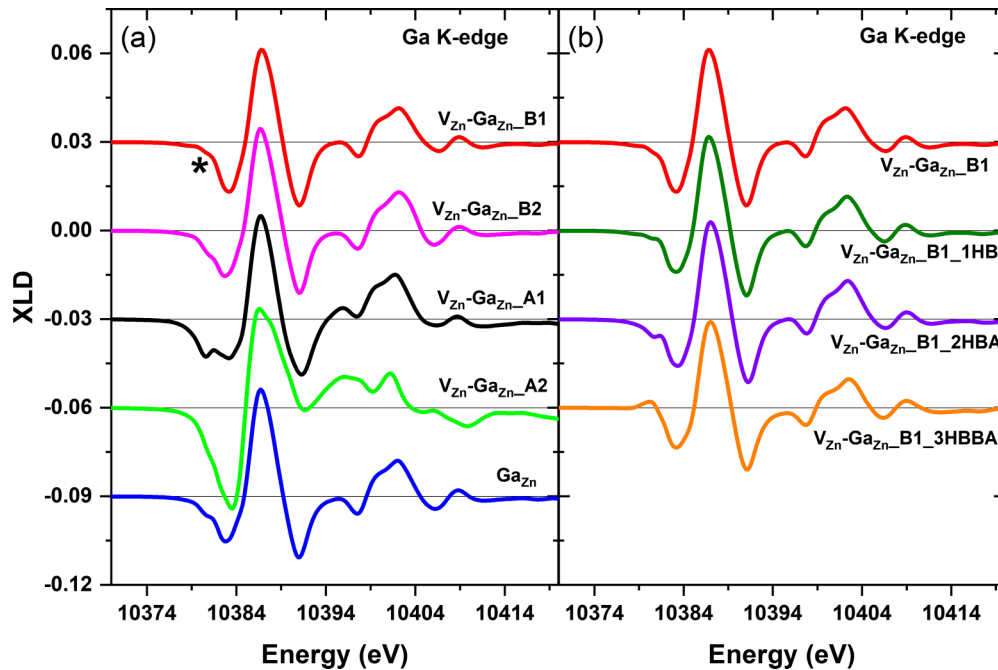


FIG. 5. (a) Simulated x-ray linear dichroism (XLD) spectra for various relaxed structural models combining one V_{Zn} in axial A1/A2 or B1/B2 positions with one Ga_{Zn} as V_{Zn} - Ga_{Zn} defect complexes. (b) Simulated XLD spectra for various relaxed structural models combining one V_{Zn} in basal B1 position with one Ga_{Zn} and the presence of one, two, or three hydrogen atoms close to V_{Zn} in axial A and/or basal B positions as V_{Zn} - Ga_{Zn} - nH defect complexes. The A1 and B1 nomenclature stands for the first coordination shell in the axial and basal positions, respectively, while the A2 and B2 nomenclature stands for the second coordination shell in the axial and basal positions, respectively. All spectra are convoluted with only the Ga core-hole lifetime.

present in the experimental XLD spectrum, whereas the intensity ratio between the peaks located at 10383 and 10391 eV is completely different for V_{Zn} - Ga_{Zn} _A2. For the cases where V_{Zn} lies in the basal B position, the modifications in the XLD spectra are less pronounced since the XANES spectra are averaged over the a - and b -basal planes to be compliant with the experimental measurements. When V_{Zn} is placed in the second coordination shell (i.e., V_{Zn} - Ga_{Zn} _B2) or even further, only minor differences are observed as compared with the XLD spectrum simulated without V_{Zn} (i.e., Ga_{Zn}). As a result, for the cases of V_{Zn} - Ga_{Zn} _B1, V_{Zn} - Ga_{Zn} _B2, and Ga_{Zn} , the intensity of the negative shoulder on the peak located at 10380 eV [marked with an asterisk in Fig. 5(a)] is less intense only for V_{Zn} - Ga_{Zn} _B1, and therefore, it reproduces better the experimental XLD spectrum, as shown in Fig. 2(b), especially in the low-energy part. Based on a linear combination of the XLD spectra of those three defects, it appears that the amount of V_{Zn} - Ga_{Zn} _B1 must be the largest one. As an intermediate conclusion, V_{Zn} should be in the first coordination shell and preferentially lie in the basal B1 position.

In addition, the simulated XLD spectra related to V_{Zn} - Ga_{Zn} _B1 with the presence of one, two, or three hydrogen atoms close to V_{Zn} are considered. In the DFT calculations, those atoms are used to saturate the O dangling bonds, and hence, the distinct basal or axial hydrogen position is considered, e.g., V_{Zn} - Ga_{Zn} _B1_2HBB, for two hydrogen atoms—both in basal positions— V_{Zn} - Ga_{Zn} _B1_2HBA, for two hydrogen atoms—one in the basal and one in the axial position. It should be noted that, when the charge is not denoted, the defect complex is considered as neutral. Figure 5(b) shows

the simulated XLD spectra for various relaxed structural models combining one single V_{Zn} in the basal position in the first coordination shell (B1) with one Ga_{Zn} and the presence of one, two, or three hydrogen atoms close to V_{Zn} . We can see that, by adding a single hydrogen atom to V_{Zn} - Ga_{Zn} _B1, the agreement with the experimental XLD spectrum is further improved in the low-energy part. The negative shoulder on the peak located at 10380 eV is rather well suppressed, allowing us to conclude that V_{Zn} - Ga_{Zn} _B1_1HB is most certainly the dominant defect complex formed. However, we cannot exclude that either all three defect complexes with one, two, or three hydrogen atoms or the ones with two and three hydrogen atoms could be equally present. Indeed, the shoulder at the low-energy part of the XLD spectrum is opposite in sign for V_{Zn} - Ga_{Zn} _B1_2HBA and V_{Zn} - Ga_{Zn} _B1_3HBBA; hence, their average is very close to V_{Zn} - Ga_{Zn} _B1_1HB and therefore may also be compatible with the experimental XLD spectrum. However, if one considers them individually, the simulated XLD spectrum for V_{Zn} - Ga_{Zn} _B1_1HB is the closest to the experimental one, as plotted in Fig. 2(b). It is worth noticing that such an investigation of hydrogen-based defect complexes is not possible when using EXAFS since this technique is not sensitive to hydrogen bonds, contrary to XLD.

The formation energies of the V_{Zn} - Ga_{Zn} - nH defect complexes as a function of the Fermi level are presented in Figs. 6(a) and 6(b) for Zn- and O-rich conditions, respectively. The study on the interaction between two V_{Zn} and one Ga_{Zn} is included in two models presented in the Supplemental Material [64]. The comparison of their formation energies

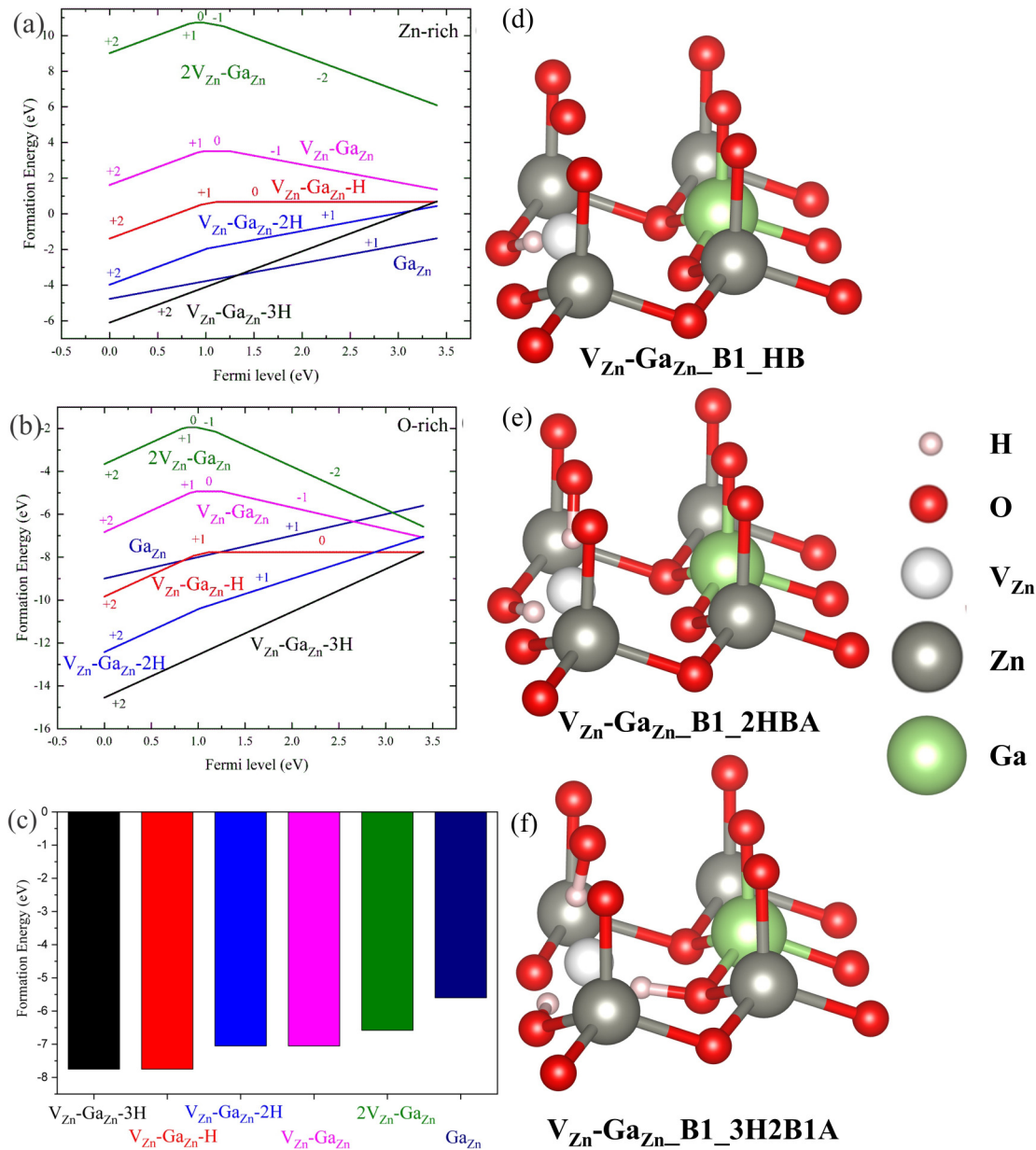


FIG. 6. Formation energies of Ga- and hydrogen-related defects in ZnO as a function of Fermi level determined by density functional theory (DFT) calculations for (a) Zn- and (b) O-rich conditions. The most stable atomic configuration with the lowest energy is presented for each charge state. The zero of Fermi energy was set at the valence band maximum (VBM). The chemical potential values of $\mu_{\text{O}} = -4.22$ eV (Zn-rich), $\mu_{\text{O}} = 0$ eV (O-rich), and $\mu_{\text{H}} = -0.475$ eV were used. (c) Formation energies of the different Ga- and hydrogen-related defects for O-rich conditions considering the Fermi level close to the conduction band minimum (CBM). (d)–(f) Relaxed structural models for the most stable atomistic configurations of the $V_{\text{Zn}}\text{-Ga}_{\text{Zn}}\text{-}n\text{H}$ -related defect complexes having the Ga dopant in the basal position with respect to V_{Zn} . In (d), the basal $V_{\text{Zn}}\text{-Ga}_{\text{Zn}}\text{-B1_HB}$ defect complex is given with one hydrogen atom saturating an oxygen dangling bond in the basal position. In (e), the $V_{\text{Zn}}\text{-Ga}_{\text{Zn}}\text{-B1_2HBA}$ defect complex is provided with two hydrogens, one in the basal position and one in the axial position. In (f), the $V_{\text{Zn}}\text{-Ga}_{\text{Zn}}\text{-B1_3H2B1A}$ defect complex is given with three hydrogens, two hydrogens in the basal position, and one in the axial position. Large gray balls, small red balls, and large green balls denote Zn, O, and Ga atoms, respectively. Small pink balls are hydrogen atoms. For the sake of clarity, the position of the V_{Zn} is represented with a white ball.

reveals that the model presented in the Supplemental Material [64] is the favorable one. However, as seen in Figs. 6(a) and 6(b), the $2V_{\text{Zn}}\text{-Ga}_{\text{Zn}}$ defect complex is energetically unfavorable with respect to the rest of the investigated structural models except for O-rich conditions with the Fermi level close to the CBM for which the required formation energy excess is less. The $2\text{Ga}_{\text{Zn}}\text{-V}_{\text{Zn}}$ defect complex is not considered in

the present DFT and XLD simulations since V_{Zn} 's are more mobile thanks to their lower formation energy and smaller activation energy for diffusion than Ga dopants in ZnO. Consequently, they can much more easily form V_{Zn} clusters. Ga dopants in ZnO are more likely to be immobile or exhibit limited mobility, especially at low doping concentrations and low temperatures, due to their larger size and higher activation

energy for diffusion [65]. Recently, it has been denoted that the formation of the $2Ga_{Zn}-V_{Zn}$ defect complex is challenging due to the need for Ga dopants to diffuse. The Ga-dopant diffusion is slower than the Zn self-diffusion because of the low impurity to host-cation ratio [66].

For Zn-rich conditions with the Fermi level close to the CBM, Ga_{Zn} has the lowest formation energy and acts as a shallow donor. The $V_{Zn}-Ga_{Zn}-3H$ defect complex with a +2 charge state as a shallow donor as well is energetically favorable only when the Fermi level is close to the VBM. The rest of the defect complexes related to V_{Zn} and Ga_{Zn} require an energy excess of >1.5 eV to be formed. Interestingly, it should be noted that starting from Zn- toward O-rich conditions, the formation energies of defect complexes related to V_{Zn} and Ga_{Zn} are lowered with respect to the formation energy of single Ga_{Zn} . Importantly, intermediate and O-rich conditions should be considered during the CBD of ZnO NWs [67]. The need for placing the CBD of ZnO NWs in a high pH region to efficiently incorporate Ga dopants using attractive electrostatic forces in the chemical bath corresponds to more oxidizing and hence O-rich conditions [31]. For O-rich conditions with the Fermi level close to the CBM as expected for ZnO NWs grown by CBD [67], all the defects and defect complexes related to V_{Zn} and Ga_{Zn} are energetically favorable, as seen in Fig. 6(c). The $V_{Zn}-Ga_{Zn}$ defect complex with a -1 charge state acting as a deep acceptor is specifically more favorable energetically than single Ga_{Zn} , as reported in Ref. [34]. However, the hydrogen-passivated $V_{Zn}-Ga_{Zn}$ defect complexes ($V_{Zn}-Ga_{Zn}-nH$) in the form of $V_{Zn}-Ga_{Zn}-H$, $V_{Zn}-Ga_{Zn}-2H$, and $V_{Zn}-Ga_{Zn}-3H$, as represented in Figs. 6(d)–6(f), should be considered by far dominant even with the Fermi level in the middle of the band gap. Here, $V_{Zn}-Ga_{Zn}-H$ with a zero charge state acting as a neutral complex and $V_{Zn}-Ga_{Zn}-3H$ with a +2 charge state acting as a doubly ionized shallow donor have the lowest formation energy. In contrast, the formation energy of $V_{Zn}-Ga_{Zn}-2H$ with a +1 charge state acting as a singly ionized shallow donor is slightly higher. In other words, the family of $V_{Zn}-Ga_{Zn}-nH$ defect complexes overall provides a large amount of free electrons to Ga-doped ZnO NWs grown by CBD and thus accounts for their high electrical conductivity with a free electron density ranging from 3.10×10^{18} to $9.00 \times 10^{19} \text{ cm}^{-3}$, as measured by scanning spreading resistance microscopy in Ref. [68]. This mainly originates from the massive incorporation of $V_{Zn}-Ga_{Zn}-2H$ and $V_{Zn}-Ga_{Zn}-3H$ defect complexes. The $V_{Zn}-Ga_{Zn}-H$ defect complex is instead electrically inactive despite its high concentration, meaning that the incorporation of hydrogen and Ga dopants during the CBD of ZnO NWs is of the same order of magnitude. Hydrogen acts as an efficient passivating species even when an intentional dopant is used during the CBD process. These findings show that the residual and intentional doping processes are highly correlated

and that any optimization of the optical and electrical properties of ZnO NWs grown by CBD should consider significant interplay effects between the hydrogen and intentional dopants.

IV. CONCLUSIONS

In summary, the XLD spectra of Ga-doped ZnO NWs grown by CBD using synchrotron-based x-ray radiation coupled with DFT calculations reveal that the family of $V_{Zn}-Ga_{Zn}-nH$ defect complexes is predominantly formed. The $V_{Zn}-Ga_{Zn}-2H$ and $V_{Zn}-Ga_{Zn}-3H$ defect complexes acting as two singly and doubly shallow donors, respectively, account for the high electrical conductivity of Ga-doped ZnO NWs, although the $V_{Zn}-Ga_{Zn}-H$ defect complex as a neutral complex presents the highest concentration. These findings revisit the nature of intentional dopant-induced defects and defect complexes in ZnO NWs grown by CBD. They further emphasize that the residual and intentional doping processes are highly correlated through significant interplay effects. Hydrogen is found to act as an efficient passivating species, even for intentional dopants like Ga. Eventually, hydrogen should be considered in unintentionally doped ZnO NWs grown by CBD as major defects for tuning their optical and electrical properties but also in intentionally doped ZnO NWs through their efficient passivating effect.

ACKNOWLEDGMENTS

The authors thank Odette Chaix-Pluchery, Isabelle Gélard, and Laetitia Rapenne from LMGP, Grenoble, France, for their assistance in Raman scattering and EDS measurements, respectively. The authors warmly thank Yves Joly from Institut Néel, Grenoble, France, for implementing the exchange-correlation potential PBE96 in the FDMNES code. The authors acknowledge the financial support by the French National Research Agency through the projects DOSETTE (No. ANR-17-CE24-0004) and ROLLER (No. ANR-17-CE09-0033). P.G. was supported by a doctoral fellowship from the CDP Eco-SESA (No. ANR-15-IDEX-02). The authors further acknowledge the ESRF synchrotron for the provision of beamtime and the facilities, and the scientific and technical assistance of CMTIC characterization platform of Grenoble INP, which is supported by the Centre of Excellence of Multifunctional Architected Materials (LabEx CEMAM) under Contract No. ANR-10-LABX-44-01 funded by the “Investments for the Future” Program. This paper further benefited from the CIMENT/GRICAD platform in Grenoble for computational resources as well as by computational time granted from Greek Research & Technology Network in ARIS National HPC infrastructure under Project NOUS (pr012041).

- [1] L. Vayssieres, K. Keis, S. E. Lindquist, and A. Hagfeldt, *J. Phys. Chem. B* **105**, 3350 (2001).
 [2] L. Vayssieres, *Adv. Mater.* **15**, 464 (2003).

- [3] D. Vanmaekelbergh and L. K. van Vugt, *Nanoscale* **3**, 2783 (2011).
 [4] F. Rahman, *Opt. Eng.* **58**, 010901 (2019).

- [5] W. Ouyang, J. Chen, Z. Shi, and X. Fang, *Appl. Phys. Rev.* **8**, 031315 (2021).
- [6] V. Consonni, J. Briscoe, E. Karber, X. Li, and T. Cossuet, *Nanotechnology* **30**, 362001 (2019).
- [7] J. Briscoe and S. Dunn, *Nano Energy* **14**, 15 (2015).
- [8] J. Liu, Y. Wang, J. Ma, Y. Peng, and A. Wang, *J. Alloys Compd.* **783**, 898 (2019).
- [9] A. Mirzaei, J.-H. Lee, S. M. Majhi, M. Weber, M. Bechelany, H. W. Kim, and S. S. Kim, *J. Appl. Phys.* **126**, 241102 (2019).
- [10] D. Lincot, *MRS Bull.* **35**, 778 (2010).
- [11] S. Xu and Z. L. Wang, *Nano Res.* **4**, 1013 (2011).
- [12] A. Janotti and C. G. Van de Walle, *Rep. Prog. Phys.* **72**, 126501 (2009).
- [13] M. D. McCluskey and S. J. Jokela, *J. Appl. Phys.* **106**, 071101 (2009).
- [14] F. Tuomisto, V. Ranki, K. Saarinen, and D. C. Look, *Phys. Rev. Lett.* **91**, 205502 (2003).
- [15] A. Janotti and C. G. Van de Walle, *Phys. Rev. B* **76**, 165202 (2007).
- [16] X. J. Wang, L. S. Vlasenko, S. J. Pearton, W. M. Chen, and I. A. Buyanova, *J. Phys. D Appl. Phys.* **42**, 175411 (2009).
- [17] C. G. Van de Walle, *Phys. Rev. Lett.* **85**, 1012 (2000).
- [18] A. Janotti and C. G. Van de Walle, *Nat. Mater.* **6**, 44 (2007).
- [19] D. M. Hofmann, A. Hofstaetter, F. Leiter, H. J. Zhou, F. Henecker, B. K. Meyer, S. B. Orlinskii, J. Schmidt, and P. G. Baranov, *Phys. Rev. Lett.* **88**, 045504 (2002).
- [20] J. L. Lyons, J. B. Varley, D. Steiauf, A. Janotti, and C. G. Van de Walle, *J. Appl. Phys.* **122**, 035704 (2017).
- [21] Y. K. Frodason, K. M. Johansen, T. S. Bjorheim, B. G. Svensson, and A. Alkauskas, *Phys. Rev. B* **97**, 104109 (2018).
- [22] J. Villafuerte, F. Donatini, J. Kioseoglou, E. Sarigiannidou, O. Chaix-Pluchery, J. Pernot, and V. Consonni, *J. Phys. Chem. C* **124**, 16652 (2020).
- [23] X. N. Li, B. Keyes, S. Asher, S. B. Zhang, S. H. Wei, T. J. Coutts, S. Limpijumngong, and C. G. Van de Walle, *Appl. Phys. Lett.* **86**, 122107 (2005).
- [24] S. J. Jokela and M. D. McCluskey, *Phys. Rev. B* **76**, 193201 (2007).
- [25] M. N. Amini, R. Saniz, D. Lamoen, and B. Partoens, *Phys. Chem. Chem. Phys.* **17**, 5485 (2015).
- [26] D. Y. Yong, H. Y. He, Z. K. Tang, S. H. Wei, and B. C. Pan, *Phys. Rev. B* **92**, 235207 (2015).
- [27] J. Villafuerte, O. Chaix-Pluchery, J. Kioseoglou, F. Donatini, E. Sarigiannidou, J. Pernot, and V. Consonni, *Phys. Rev. Mater.* **5**, 056001 (2021).
- [28] X. H. Huang, Z. Y. Zhan, K. P. Pramoda, C. Zhang, L. X. Zheng, and S. J. Chua, *Crystengcomm* **14**, 5163 (2012).
- [29] E. G. Barbagiovanni, R. Reitano, G. Franzo, V. Strano, A. Terrasi, and S. Mirabella, *Nanoscale* **8**, 995 (2016).
- [30] C. Verrier, E. Appert, O. Chaix-Pluchery, L. Rapenne, Q. Rafhay, A. Kaminski-Cachopo, and V. Consonni, *Inorg. Chem.* **56**, 13111 (2017).
- [31] P. Gaffuri, E. Appert, O. Chaix-Pluchery, L. Rapenne, M. Salaun, and V. Consonni, *Inorg. Chem.* **58**, 10269 (2019).
- [32] C. Lausecker, B. Salem, X. Baillin, O. Chaix-Pluchery, H. Roussel, S. Labau, B. Pelissier, E. Appert, and V. Consonni, *Inorg. Chem.* **60**, 1612 (2021).
- [33] F. Wang, J.-H. Seo, D. Bayerl, J. Shi, H. Mi, Z. Ma, D. Zhao, Y. Shuai, W. Zhou, and X. Wang, *Nanotechnology* **22**, 225602 (2011).
- [34] D. O. Demchenko, B. Earles, H. Y. Liu, V. Avrutin, N. Izyumskaya, Ü. Özgür, and H. Morkoç, *Phys. Rev. B* **84**, 075201 (2011).
- [35] H. Wang, S. Baek, J. Song, J. Lee, and S. Lim, *Nanotechnology* **19**, 075607 (2008).
- [36] A. Escobedo-Morales and U. Pal, *Appl. Phys. Lett.* **93**, 193120 (2008).
- [37] G. Pineda-Hernández, A. Escobedo-Morales, U. Pal, and E. Chigo-Anota, *Mater. Chem. Phys.* **135**, 810 (2012).
- [38] G. C. Park, S. M. Hwang, J. H. Lim, and J. Joo, *Nanoscale* **6**, 1840 (2014).
- [39] R. Li, C. Yu, H. Dong, W. Jia, T. Li, Z. Zhang, and B. Xu, *RSC Adv.* **7**, 49613 (2017).
- [40] G. Ciatto, A. Di Trollo, E. Fonda, P. Alippi, A. M. Testa, and A. A. Bonapasta, *Phys. Rev. Lett.* **107**, 127206 (2011).
- [41] Q. Ma, J. T. Prater, C. Sudakar, R. A. Rosenberg, and J. Narayan, *J. Phys.: Condens. Matter* **24**, 306002 (2012).
- [42] E. Sarigiannidou, F. Wilhelm, E. Monroy, R. M. Galera, E. Bellet-Amalric, A. Rogalev, J. Goulon, J. Cibert, and H. Mariette, *Phys. Rev. B* **74**, 041306(R) (2006).
- [43] A. Ney, K. Ollefs, S. Ye, T. Kammermeier, V. Ney, T. C. Kaspar, S. A. Chambers, F. Wilhelm, and A. Rogalev, *Phys. Rev. Lett.* **100**, 157201 (2008).
- [44] A. Rogalev and F. Wilhelm, *Phys. Met. Metall.* **116**, 1285 (2015).
- [45] O. Bunău and Y. Joly, *J. Phys.: Condens. Matter* **21**, 345501 (2009).
- [46] S. A. Guda, A. A. Guda, M. A. Soldatov, K. A. Lomachenko, A. L. Bugaev, C. Lamberti, W. Gawelda, C. Bressler, G. Smolentsev, A. V. Soldatov and Y. Joly, *J. Chem. Theory Comput.* **11**, 4512 (2015).
- [47] G. Kresse and J. Furthmüller, *Phys. Rev. B* **54**, 11169 (1996).
- [48] G. Kresse and D. Joubert, *Phys. Rev. B* **59**, 1758 (1999).
- [49] P. E. Blochl, *Phys. Rev. B* **50**, 17953 (1994).
- [50] J. P. Perdew, K. Burke, and M. Ernzerhof, *Phys. Rev. Lett.* **77**, 3865 (1996).
- [51] J. P. Perdew, K. Burke, and M. Ernzerhof, *Phys. Rev. Lett.* **78**, 1396(E) (1997).
- [52] S. L. Dudarev, G. A. Botton, S. Y. Savrasov, C. J. Humphreys, and A. P. Sutton, *Phys. Rev. B* **57**, 1505 (1998).
- [53] P. Erhart, K. Albe, and A. Klein, *Phys. Rev. B* **73**, 205203 (2006).
- [54] N. N. Lathiotakis, A. N. Andriotis, and M. Menon, *Phys. Rev. B* **78**, 193311 (2008).
- [55] R. M. Sheetz, I. Ponomareva, E. Richter, A. N. Andriotis, and M. Menon, *Phys. Rev. B* **80**, 195314 (2009).
- [56] Q. B. Wang, C. Zhou, J. Wu, and T. Lu, *Opt. Commun.* **297**, 79 (2013).
- [57] L. Dong, R. Jia, B. Xin, B. Peng, and Y. Zhang, *Sci. Rep.* **7**, 40160 (2017).
- [58] J. L. Lyons, A. Janotti, and C. G. Van de Walle, *Phys. Rev. B* **80**, 205113 (2009).
- [59] C. Freysoldt, B. Grabowski, T. Hickel, J. Neugebauer, G. Kresse, A. Janotti, and C. G. Van de Walle, *Rev. Mod. Phys.* **86**, 253 (2014).
- [60] G.-Y. Huang, C.-Y. Wang, and J.-T. Wang, *Physica B* **405**, 158 (2010).
- [61] H. F. McMurdie, M. C. Morris, E. H. Evans, B. Paretzkin, W. Wong-Ng, L. Ettliger, and C. R. Hubbard, *Powder Diffr.* **1**, 64 (2013).

- [62] H. Karzel, W. Potzel, M. Köfferlein, W. Schiessl, M. Steiner, U. Hiller, G. M. Kalvius, D. W. Mitchell, T. P. Das, P. Blaha, K. Schwarz, and M. P. Pasternak, *Phys. Rev. B* **53**, 11425 (1996).
- [63] A. Ney, V. Ney, K. Ollefs, D. Schauries, F. Wilhelm, and A. Rogalev, *J. Surf. Interfaces Mater.* **2**, 14 (2014).
- [64] See Supplemental Material at <http://link.aps.org/supplemental/10.1103/PhysRevMaterials.7.076001> for Zn and Ga K-edges XANES spectra as measured with TFY and shown in Fig. SM1. In Fig. SM2(a), both vacancies and the Ga substitutional atom are in the same basal plane, while the Ga atom is between vacancies. In Fig. SM2(b), in comparison with the previous model, one vacancy is located on the upper layer, and hence, they are not in the same basal plane. Large gray balls, small red balls, and large green balls denote zinc, oxygen, and gallium atoms, respectively. The energetically favorable is the one in Fig. SM2(a).
- [65] D. Steiauf, J. L. Lyons, A. Janotti, and C. G. Van de Walle, *APL Mater.* **2**, 096101 (2014).
- [66] Y. Ke, S. Lany, J. J. Berry, J. D. Perkins, P. A. Parilla, A. Zakutayev, T. Ohno, R. O'Hayre, and D. S. Ginley, *Adv. Funct. Mater.* **24**, 2875 (2014).
- [67] J. Villafuerte, E. Sarigiannidou, F. Donatini, J. Kioseoglou, O. Chaix-Pluchery, J. Pernot, and V. Consonni, *Nanoscale Adv.* **4**, 1793 (2022).
- [68] O. Synhaivskyi, D. Albertini, P. Gaffuri, J.-M. Chauveau, V. Consonni, B. Gautier, and G. Bremond, *J. Phys. Chem. C* **125**, 15373 (2021).